

Origin of High Ionic Conductivity of Sc-Doped Sodium-Rich NASICON Solid-State Electrolytes

Fei Sun, Yuxuan Xiang, Qian Sun, Guiming Zhong, Mohammad Norouzi Banis, Yulong Liu, Ruying Li, Riqiang Fu, Matthew Zheng, Tsun-Kong Sham,* Yong Yang,* Xuhui Sun,* and Xueliang Sun*

Substitution of liquid electrolyte with solid-state electrolytes (SSEs) has emerged as a very urgent and challenging research area of rechargeable batteries. NASICON ($\text{Na}_3\text{Zr}_2\text{Si}_2\text{PO}_{12}$) is one of the most potential SSEs for Na-ion batteries due to its high ionic conductivity and low thermal expansion. It is proven that the ionic conductivity of NASICON can be improved to $10^{-3} \text{ S cm}^{-1}$ by Sc-doping, of which the mechanism, however, has not been fully understood. Herein, a series of $\text{Na}_{3+x}\text{Sc}_x\text{Zr}_{2-x}\text{Si}_2\text{PO}_{12}$ ($0 \leq x \leq 0.5$) SSEs are prepared. To gain a deep insight into the ion transportation mechanism, synchrotron-based X-ray absorption spectroscopy (XAS) is employed to characterize the electronic structure, and solid-state nuclear magnetic resonance (SS-NMR) is used to analyze the dynamics. In this study, Sc is successfully doped into $\text{Na}_3\text{Zr}_2\text{Si}_2\text{PO}_{12}$ to substitute Zr atoms. The redistribution of sodium ions at certain specific sites is proven to be critical for sodium ion movement. For $x \leq 0.3$, the promotion of sodium ion movement is attributed to sodium ion concentration increase at the Na2 sites and decrease at the Na1 and Na3 sites. For $x > 0.3$, the inhibition of sodium ion movement is due to the phase change from monoclinic to rhombohedral and an increasing impurity content.

1. Introduction

With superior reliability and energy conversion efficiency, rechargeable batteries are one of the most promising storage technologies for sustainable energy. Na-ion batteries (NIBs) are considered as the most promising candidates to compete with

the most developed Li-ion batteries (LIBs) due to their low price, non-toxicity, and abundance.^[1–6] To improve safety and durability, as well as simplify the cell design, substituting the flammable liquid electrolytes with solid-state electrolytes (SSEs) has gained increasing attention. Moreover, solid-state NIBs can enable the usage of Na metal anode and high voltage cathodes to achieve higher energy density.^[7–10]

Among different sodium ion based SSEs, NA Super-Ionic CONductor (NASICON) with a general formula of $\text{Na}_{1+n}\text{Zr}_2\text{Si}_n\text{P}_{3-n}\text{O}_{12}$ ($1.6 \leq n \leq 2.4$), has gained the most attention due to its high ionic conductivity and low thermal expansion.^[11–18] The NASICON structure, first reported by Goodenough et al.,^[19] consists of a rigid 3D network with P/SiO₄ tetrahedral and ZrO₆ octahedral sharing the corners. The interconnected channels of the framework serve as the conduction pathway for Na⁺ ions (Figure 1a). In

general, the ionic conductivity of $\text{Na}_3\text{Zr}_2\text{Si}_2\text{PO}_{12}$ is at the level of $10^{-4} \text{ S cm}^{-1}$. To further improve it, many efforts have been made in past decades.^[10–15,18,20–25] One of the most efficient way is to substitute portion of the Zr element with other elements such as Zn, Ce, Zr, Sc, etc. Sc was reported to significantly improve the ionic conductivity of NASICON to the scale

Dr. F. Sun, Prof. X. H. Sun
Soochow University-Western University Center for Synchrotron Radiation Research
Institute of Functional Nano and Soft Materials (FUNSOM)
Jiangsu Key Laboratory for Carbon-Based Functional Materials & Devices
Soochow University
Suzhou 215123, China
E-mail: xhsun@suda.edu.cn

Dr. F. Sun, Dr. Q. Sun, Dr. M. N. Banis, Dr. Y. Liu, R. Li, M. Zheng, Prof. X. L. Sun
Department of Mechanical and Materials Engineering
University of Western Ontario
London, Ontario N6A 5B9, Canada
E-mail: xsun@eng.uwo.ca

Y. Xiang, Prof. Y. Yang
State Key Laboratory for Physical Chemistry of Solid Surfaces
Collaborative Innovation Center of Chemistry for Energy Materials and Department of Chemistry
College of Chemistry and Chemical Engineering
Xiamen University
Xiamen 361005, China
E-mail: yyang@xmu.edu.cn

Dr. G. Zhong
Xiamen Institute of Rare Earth Materials
Chinese Academy of Sciences
Xiamen 361021, China

Dr. R. Fu
National High Magnetic Field Laboratory
1800 E. Paul Dirac Drive, Tallahassee, FL 32310, USA

Prof. T.-K. Sham
Department of Chemistry
University of Western Ontario
London, Ontario N6A 5B7, Canada
E-mail: tsham@uwo.ca

The ORCID identification number(s) for the author(s) of this article can be found under <https://doi.org/10.1002/adfm.202102129>.

DOI: 10.1002/adfm.202102129

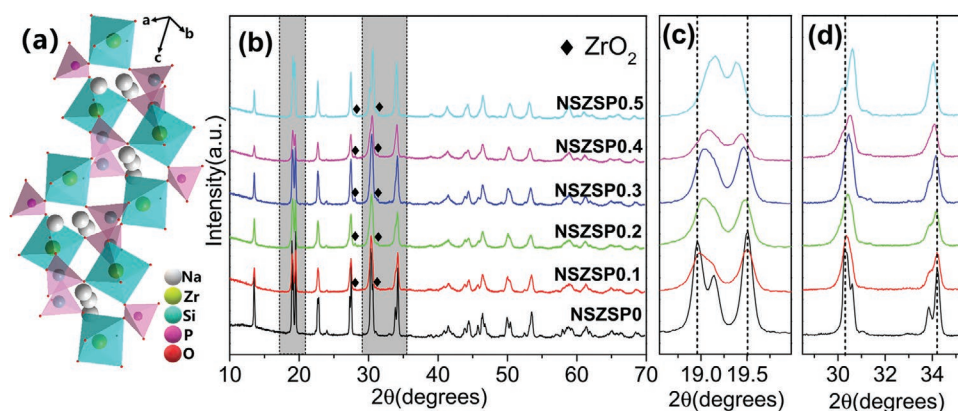


Figure 1. a) Schematic of a general NASICON structure. b) XRD patterns of NSZSP x ($x = 0, 0.1, 0.2, 0.3, 0.4, 0.5$). c,d) Magnified views of selected regions.

of $10^{-3} \text{ S cm}^{-1}$.^[12] Sc^{3+} has an ionic radius of 0.0745 nm, which is the closest to that of Zr^{4+} (0.072 nm), however, the dynamics and mechanism of Sc-doping on NASICON have not been thoroughly understood. A recent study used NMR to analyze Sc-doping on a sodium-poor NASICON $\text{Na}_3\text{Sc}_x\text{Zr}_{2-x}\text{Si}_2\text{PO}_{12}$ phase,^[20] but the sodium-poor $\text{Na}_3\text{Sc}_x\text{Zr}_{2-x}\text{Si}_2\text{PO}_{12}$ phases in this study showed relatively low ionic conductivities (around $10^{-4} \text{ S cm}^{-1}$). Another recent study investigated the ionic conducting mechanism of one sodium-rich Sc-doped NASICON.^[21] Nonetheless, the detailed understanding from a comprehensive evolution in the series of sodium-rich NASICON $\text{Na}_{3+x}\text{Sc}_x\text{Zr}_{2-x}\text{Si}_2\text{PO}_{12}$ ($0 \leq x \leq 0.5$) is still in its infancy.

In this work, in order to achieve a thorough understanding of the mechanism of sodium-rich Sc-doped NASICON phase with high ionic conductivity of $10^{-3} \text{ S cm}^{-1}$, synchrotron-based X-ray absorption spectroscopy (XAS), and solid-state nuclear magnetic resonance (SS-NMR) relaxometry are carried out to examine the electronic and local structure of elements such as P, Si, and Sc, as well as the Na^+ ion transport. Diffusion parameters including hopping rates of Na^+ ions and activation barriers for single ion jump are analyzed as well, which are directly related to the performance of these solid-state electrolytes. Insight into the mechanism and ion migration in the NASICON electrolyte can be of significance in further improving the ionic conductivity of various solid-state electrolytes in the future.

2. Results and Discussion

2.1. Crystal Structure and Morphology of the Ceramic Electrolytes

$\text{Na}_{3+x}\text{Sc}_x\text{Zr}_{2-x}\text{Si}_2\text{PO}_{12}$ (denoted as NSZSP x , where $0 \leq x \leq 0.5$) SSEs were synthesized by a sol-gel method. The NSZSP x pellets were sintered at 1250°C and polished before use. Based on the XRD result shown in Figure 1b, the NASICON-type phase $\text{Na}_{3+x}\text{Sc}_x\text{Zr}_{2-x}\text{Si}_2\text{PO}_{12}$ is the major crystalline phase of all the NSZSP x samples. Two small diffraction peaks at 28.1° and 31.4° indicates the formation of monoclinic ZrO_2 impurity which is inevitable during the synthesis of NASICON SSEs.^[26–31] Based

on previous studies, the effect of a small amount of ZrO_2 is negligible. No diffraction peak of any Sc-related impurities can be found in the XRD pattern, it is demonstrated that Sc has been successfully doped into the NASICON structure, which is consistent with some previous studies.^[12,20]

With increasing Sc-doping, the diffraction peaks at 19.1° and 30.5° slightly shift to higher angles (Figure 1c), while those at 19.5° and 34.2° shift to lower angles (Figure 1d). The two XRD peaks at around 19° become one peak as and the peak at 30.5° splits into two peaks. These observations suggest that the increasing Sc-doping change the crystal parameters, that is, from monoclinic phase to rhombohedral phase.^[12,19] Ma et al. reported that the lattice parameters a and b of the monoclinic structure increased while c decreased with Sc^{3+} substitution. For the rhombohedral structure, cell parameter a increased while c decreased. These changes might be caused by the radius difference between Zr^{4+} (0.072 nm) and Sc^{3+} (0.0745 nm), and the increased Na^+ concentration in the formula unit of sodium-rich $\text{Na}_{3+x}\text{Sc}_x\text{Zr}_{2-x}\text{Si}_2\text{PO}_{12}$.

Scanning Electron Microscope (SEM) was used to compare the microstructures of NSZSP0 (Figure 2a) and NSZSP0.3 (Figure 2b). The NASICON grain sizes of both are around 1–2 μm . The result of EDS mapping on NSZSP0.3 reveals that the distribution of elements including Sc, Na, Zr, Si, P, and O are all quite uniform (Figure 2c–h). This is basically consistent with the XRD results.

2.2. Ionic Conductivities of NSZSP x Solid Electrolytes

The ionic conductivity of pristine NSZSP0 and doped NSZSP x ($x = 0.1, 0.2, 0.3, 0.4, 0.5, 0.6$) at different temperatures were measured by electrochemical impedance spectroscopy (EIS). An Au thin film as blocking electrodes was deposited on both sides of the electrolyte pellets by sputtering. Figure 3a,b compare the Nyquist plots of the pristine NSZSP0 and the doped NSZSP x ($x = 0.1, 0.2, 0.3, 0.4, 0.5, 0.6$) at 25 and 100°C , respectively. Figure 3c shows the impedance of NSZSP0.3 from 25 to 100°C . The total conductivities of NSZSP0.3 and NSZSP0.4 are almost 4 times higher than that of the pristine NSZSP0 at 25°C . The NSZSP0 exhibits an ionic conductivity

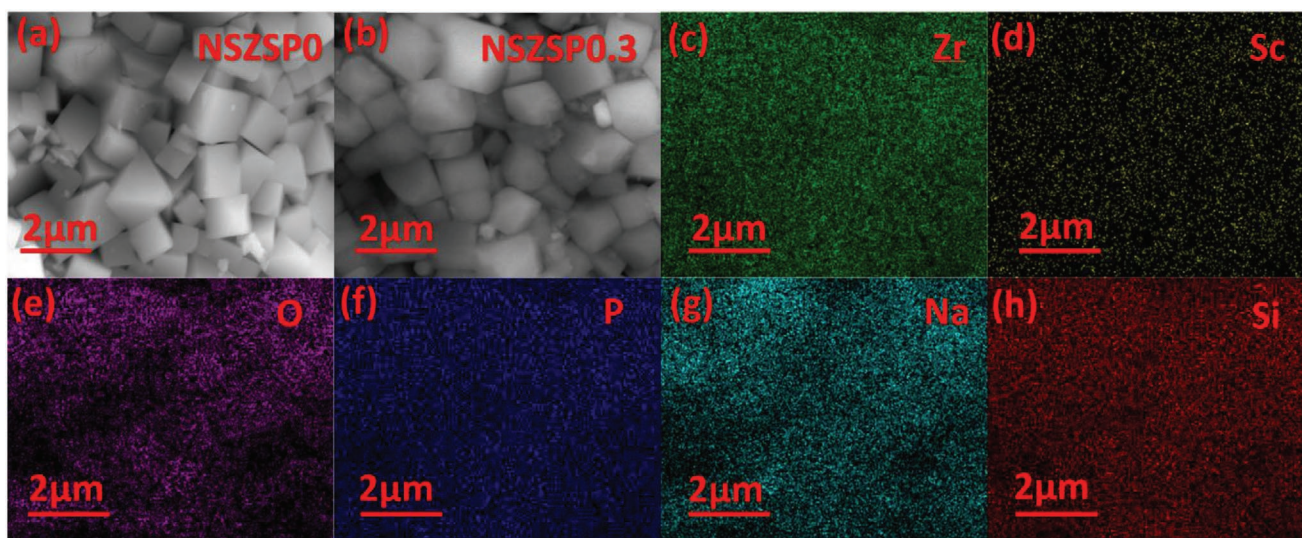


Figure 2. SEM images of a) NSZSP0 and b) NSZSP0.3. Corresponding EDS mappings of c) Zr, d) Sc, e) O, f) P, g) Na, and h) Si elements.

of $4.9 \times 10^{-4} \text{ S cm}^{-1}$ at 25 °C, which is comparable with previous results.^[10–15,18] With increasing amounts of Sc, the total ionic conductivity at 25 °C goes up to $1.9 \times 10^{-3} \text{ S cm}^{-1}$ at $x = 0.3$ and 0.4. Then, the further increase of Sc-doping leads to a decrease in total ionic conductivity. Ma et al. reported that the bulk conductivities basically showed the same increase

trend as total ionic conductivities.^[12] Arrhenius plots of the total ionic conductivity for NSZSP0 and NSZSP x electrolytes are shown in Figure 3d. The logarithm values of ionic conductivity are linear with $1/T$ within the temperature range of 25–100 °C. The total ionic conductivity of NSZSP0.3 can go up to $1.1 \times 10^{-2} \text{ S cm}^{-1}$ at 100 °C.

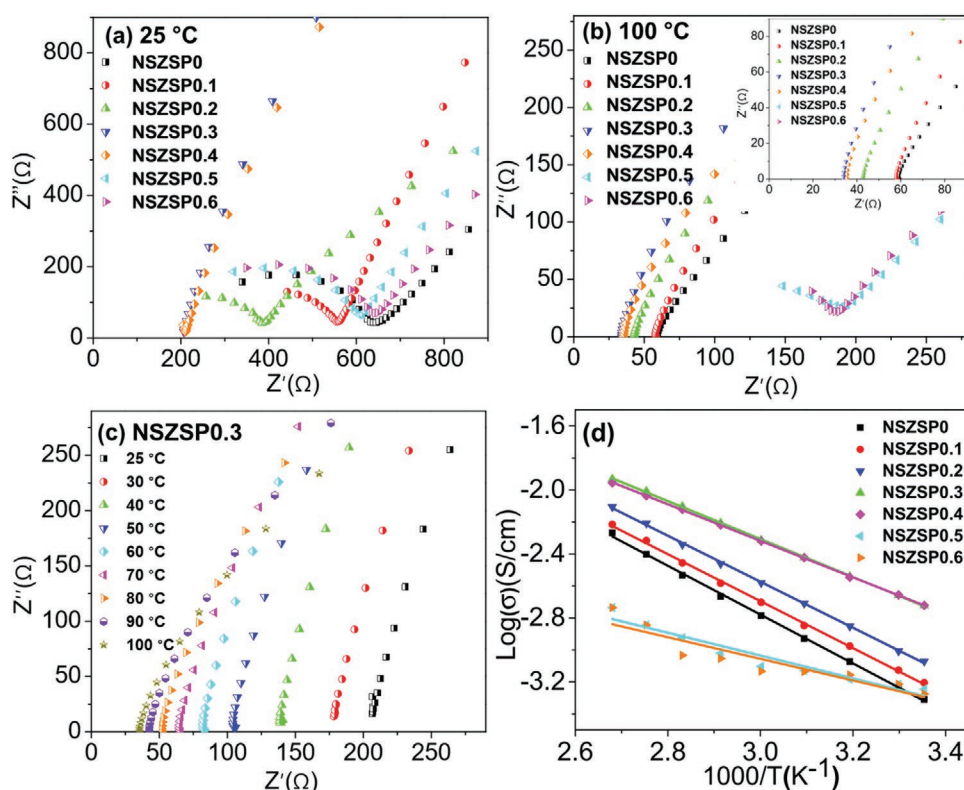


Figure 3. Temperature dependent ionic conductivities for the different NSZSP x ($x = 0, 0.1, 0.2, 0.3, 0.4, 0.5,$ and 0.6) SSEs over the temperature range from 25 to 100 °C. a) Impedance spectra of NSZSP x ($x = 0, 0.1, 0.2, 0.3, 0.4, 0.5,$ and 0.6) at 25 °C. b) Impedance spectra of NSZSP x ($x = 0, 0.1, 0.2, 0.3, 0.4, 0.5$ and 0.6) at 100 °C; the inset is a magnified view of the low impedance region. c) Impedance spectra of NSZSP0.3 at different temperatures. d) Arrhenius plots of nominal composition NSZSP x ($x = 0, 0.1, 0.2, 0.3, 0.4, 0.5,$ and 0.6) between 25 and 100 °C.

2.3. X-Ray Absorption Spectroscopy (XAS) Analysis of NSZSP x Solid Electrolytes

To unveil the ion transport mechanism of the Sc-doped NASICON with improved ionic conductivities, P K-edge, Si K-edge, and Sc $L_{3,2}$ -edge X-ray absorption spectroscopy (XAS) have been utilized for the first time to investigate the chemical environment of different elements and electronic state of NSZSP x electrolytes in the conduction band (Figure 4). The K-edge X-ray absorption near edge structure (XANES) originates from the transition of the 1s core level of an absorbing element to excited vacant states of proper symmetry involving the element p orbitals (dipole selection rules), hence the energy of the edge jump threshold and the peak intensity at the edge jump (often called the white line) are characteristic of the chemical environment, which is often understood by being compared with the standard samples. Different standard phosphate compounds have their characteristic features in main peak position as well as in the number and position of pre-edge and post-edge peaks that can be used to identify phosphate species in the XANES spectra.^[32]

Figure 4a,b shows normalized P K-edge XANES spectra of NSZSP x electrolytes with increasing x from 0 to 0.6. The main white line energy occurring near 2153.2 eV in all the P K-edge XANES can be assigned to a transition of the P 1s electron into an unoccupied valence electronic state formed by the overlap of

P sp^3 hybridization and O 2p orbitals, because the PO_4^{3-} group has Td-symmetry. A broader peak occurring at around 2169 eV dues to the multiple scattering of the tetrahedral, first shell nearest oxygen neighbors in the PO_4^{3-} group.^[23–36] All spectra, including NSZSP0, NSZSP0.2, NSZSP0.4, and NSZSP0.6 almost entirely overlap. A tiny variation on the left shoulder is due to a minute quantity of impurity containing P, which is confirmed by the following SS-NMR analysis. It can be seen that, with an increasing x , both the white line peak and the pre-edge around 2150 eV decreases gradually, which is the result of the structural change of NASICON, e.g., parameter, ligand-field, centrosymmetry or spin-states. These changes indicate a small distortion as the initially perfect sp^3 becomes distorted.

For Si K-edge (Figure 4c), all spectra overlap well with no apparent new peak or peak shift, implying that Si local structure is essentially intact. The slight variation of Si K-edge may be caused by the change of secondary structure beyond the first sphere as seen in the XRD analysis. The P K-edge and Si K-edge XANES analysis indicates that there is no apparent change on the electronic states of P and Si. Most P and Si occupy the center of the tetrahedron in NSZSP x , as is apparent from the similarity of the XANES for both elements in the tetrahedral environment of oxygen. In addition, Sc $L_{3,2}$ -edge spectra (Figure 4d) are clearly intensified along with the increasing Sc-doping amount. These spectra probe the unoccupied d states ($2p_{3/2,1/2}$ to $3d_{5/2,3/2}$ transitions) with strong perturbation from

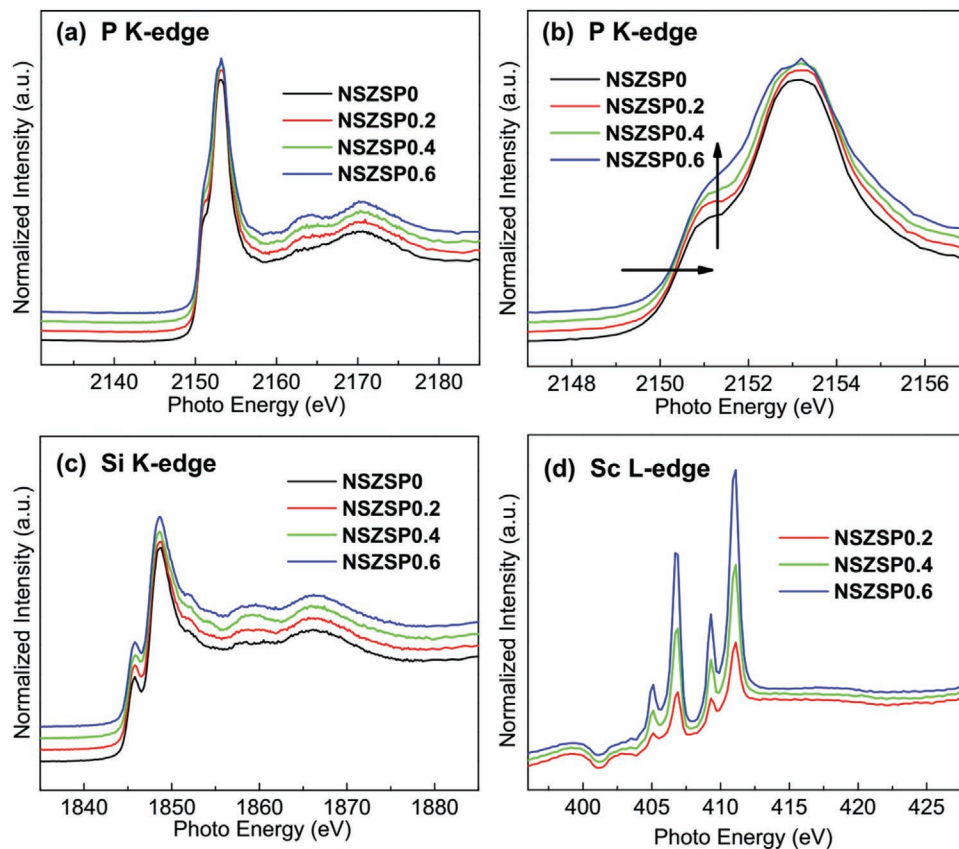


Figure 4. a) P K-edge XANES spectra for NSZSP x ($x = 0, 0.2, 0.4,$ and 0.6) SSEs. b) A magnified view of the low photo energy region in P K-edge spectra. c) Si K-edge XANES spectra for NSZSP x ($x = 0, 0.2, 0.4,$ and 0.6) SSEs. d) Sc L-edge XANES spectra for NSZSP x ($x = 0.2, 0.4,$ and 0.6) SSEs.

spin orbit coupling and crystal field effects. Meanwhile, no shift of these peaks or appearance of any new peak prove that there is no impurities containing Sc in NSZSP x . The XANES analysis, which is consistent with XRD, SEM and EDS mapping results, indicates that the Sc has been successfully doped in to NASICON to substitute Zr, leading to the observed structure change.

2.4. Solid-State Nuclear Magnetic Resonance (SS-NMR)

Solid-state nuclear magnetic resonance (SS-NMR) is a powerful tool to investigate the local structure and microscopic diffusion parameters such as hopping rates of mobile ions and activation barriers for single ion jump, with a time scale slower than X-ray absorption. To study the mechanism and ion migration in NASICON, NMR was conducted to characterize the local structure and the Na dynamics at different Na sites.

Multinuclear ^{23}Na , ^{31}P , and ^{29}Si MAS NMR spectra are shown in Figure 5a–c, respectively. High field ^{23}Na MAS NMR spectra clearly show two signals centered at the -10.5 ppm (peak 1) and -7.5 ppm (peak 2) for all compositions, as indicated through deconvolution shown in Figure 6. Peak 1 can be assigned to the main phase, which contains all three sodium sites which cannot be resolved by ultrahigh magnetic field, signaling the fast exchange between these three sodium sites in the NSZSPs lattice. Peak 2 (centered at 7.5 ppm) shows a tiny integral intensity (10%), it does not correspond to any sodium sites within the NSZSP0 lattice. Thus, Peak 2 is ascribed to impurity phase. No significant change in the spectra line-shape is observed until x is larger than 0.3. After that, at around 0 ppm, a slightly broaden line shape is observed, suggesting that the local structure of the Na^+ ion has changed with excessive scandium ions.

In the ^{31}P MAS NMR spectra of NSZSP x ($x = 0, 0.1, 0.2, 0.3, 0.4, 0.5$), each line contains two peaks centered at -11 and 6 ppm. The strong peak at -11 ppm is ascribed to the main phase of NSZSP0, while the small peaks (ranged from -5 ppm

to 10 ppm) are assigned to the impurities formed during the synthesis. ^{31}P and ^{23}Na MAS NMR spectra indicate that no significant change in line shape when $x \leq 0.3$, while for $x > 0.3$ samples, the impurity-peak increases in ^{31}P MAS NMR spectra, with a new signal emerging at around 0 ppm in ^{23}Na MAS NMR spectra, suggesting that increasing the contents of scandium ions can cause the formation of more impurities. However, no impurity is found in the ^{29}Si NMR spectra, suggesting complete incorporation of Si into the main phase. Therefore, the multinuclear NMR spectra demonstrate that Sc can be easily doped into a crystal lattice in a $x \leq 0.3$ regime. However, in a $x > 0.3$ regime, the formation of impurities that only consist of Na and P suggest that Sc may be difficult to incorporate into the main phase.

T_1 relaxometry is a common method to study the ionic motion in solid-state electrolytes. For most solids, the smaller value of T_1 denotes a faster movement of the nucleus studied. The inversion recovery experiment was herein performed to probe the dynamics of sodium ions. The curves of integral intensity against the delay time were deconvoluted by three components, according to the different T_1 values, namely SLOW (S), FAST (F), and Ultraslow (US). All curves are well fitted with these three components (Section S1, Supporting Information). Figure 7 shows the specific fitting results.

$T_1(\text{US})$ value is around 10^{-2} s, which is much bigger than the others ($\approx 10^{-4}$ s), demonstrating that the US component has a much slower motion of sodium ions. Furthermore, the ratio of this component is relatively small (10%). This ratio is the same as the contents of impurities from ^{23}Na and ^{31}P quantitative results (Figure S2, Supporting Information). Therefore, the US component is assigned to the impurities. The other two components correspond to different sodium ions in the main phase of NASICON. In order to further understand the mechanism of Sc-doping, we attribute these two components to different crystallographic sites: 1) from the XRD refinements results, the occupancy of different crystallographic sites of sodium ions is 1:1:1 in NSZSP0, while the ratio of the F component and the

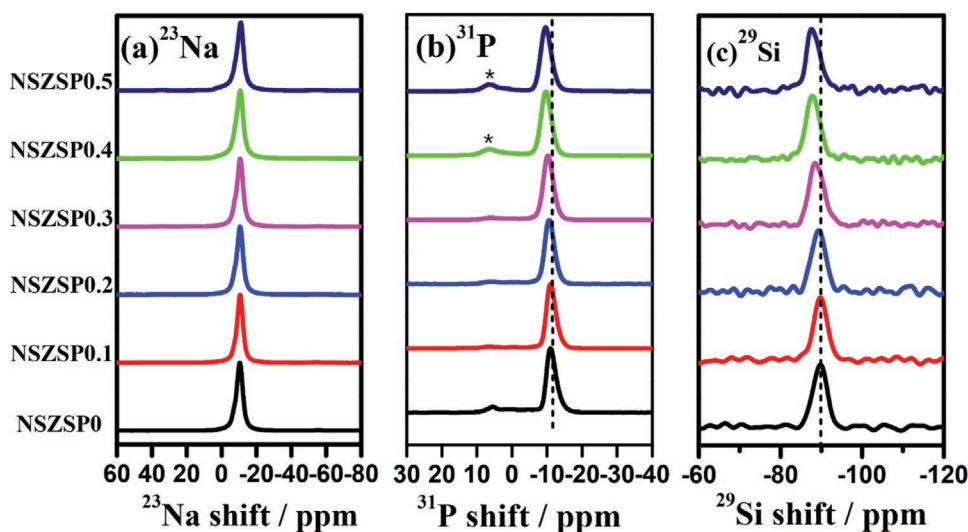


Figure 5. a) ^{23}Na MAS NMR spectra of NSZSP x ($x = 0, 0.1, 0.2, 0.3, 0.4,$ and 0.5) acquired at 21.1T. b) ^{31}P MAS NMR spectra of NSZSP x ($x = 0, 0.1, 0.2, 0.3, 0.4,$ and 0.5) at 9.4T; peaks marked by * indicate the impurities. c) ^{29}Si MAS NMR spectra of NSZSP x ($x = 0, 0.1, 0.2, 0.3, 0.4,$ and 0.5) at 9.4T.

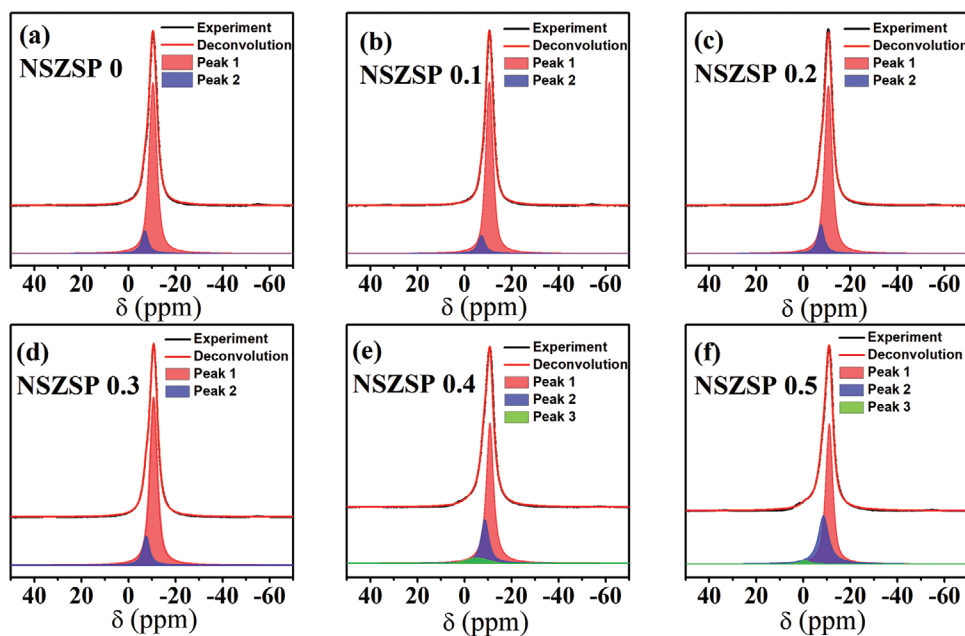


Figure 6. a–f) The deconvolution results of ^{23}Na MAS NMR spectra of NSZSP x ($x = 0, 0.1, 0.2, 0.3, 0.4,$ and 0.5) obtained at 21.1T.

S component is about 2:1. It seems that there are two sodium sites overlap in the F component; 2) as for local structure, Na1 and Na3 have the same coordination number with 6 oxygen atoms while Na2 has 8 oxygen atoms. Thus, Na1 and Na3 have the same coordination number and may overlap in one component; 3) Park et al.^[27] reported that the smallest transport bottleneck of sodium ions in NSZSP0 was close to the Na2 sites, which restrained the mobility of Na2. Based on these three aspects discussed above, we ascribe the S component to Na2 sites and the F component to the overlap of Na1 and Na3 sites. Specific assignments are shown in Figure 7.

In addition, Figure 7a shows $T_1(\text{Na2})$ and $T_1(\text{Na1 and Na3})$ reach the minimum at $x = 0.3$, representing that the transport of sodium ions is enhanced when $x \leq 0.3$, and then restrained. Therefore, the best composition is $\text{Na}_{3.3}\text{Sc}_{0.3}\text{Zr}_{1.7}\text{Si}_2\text{PO}_{12}$. It is noteworthy that the integral intensity also behaves normally for the main phase, which demonstrates that the incorporation of Sc affects the distribution of sodium ions at different chemical sites, resulting in more Na^+ with a faster transfer rate at favorable sites. In the $x \leq 0.3$ regime, with Sc^{3+} incorporating into NSZSP0, the excess Na ions prefer occupying the Na2 sites, as seen from the increase of Na2 integral intensity. At the

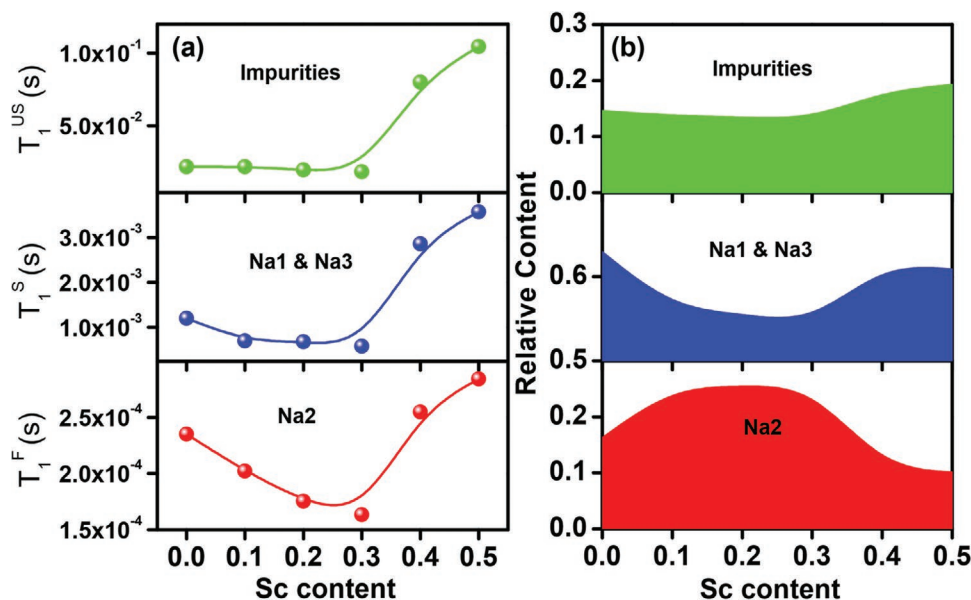


Figure 7. a) The fitting results of T_1 relaxation time for NSZSP x ($x = 0, 0.1, 0.2, 0.3, 0.4,$ and 0.5). b) Relative contents of the impurities, Na1 and Na3, and Na2 in the NSZSP x ($x = 0, 0.1, 0.2, 0.3, 0.4,$ and 0.5).

same time, the contents of sodium ions in Na1 and Na3 sites decrease. This means that Sc doping has caused a different distribution of sodium ions within the NSZSP0 structure. This is also found in Li-based NASICON-type solid-state electrolyte LATP, in which this distribution caused by element doping is considered as the true reason for the enhancement of ionic conductivity.

In the $x > 0.3$ regime, the T_1 time increases for all three components, indicating that the sodium ion motion slows down with excessive Sc^{3+} , which is consistent with the EIS results. Figure 7b shows that the amount of Na2 declines while Na1 and Na3 rise. Combined with XRD results, a phase change occurred when $x > 0.3$ can give rise to this discrepancy in different chemical sites. Ma et al.^[12] have done XRD refinements on Sc-doping NSZSP x , which show that the phase change from monoclinic phase to rhombohedral phase can lead to a decline in Na2 occupancy. This result is consistent with the T_1 fitting results reported here. Thus, it is reasonable to connect the decline in Na2 occupancy with the phase change.

Based on the above analysis, we ascribe the enhancement of ionic motion to the distribution of sodium ions at different sites. At solid-solution area ($x \leq 0.3$), Sc-doping brings excessive sodium ions which prefer occupying Na2 sites, decreasing the amount of Na1 and Na3. After $x = 0.3$, the phase change causes the occupancy of Na2 to decrease again, along with the increase in Na1 and Na3 occupancy. Such a mechanism makes the optimal sodium ion ratio appear at $x = 0.3$, which has the fastest ion mobility.

Compared to the previously reported sodium-poor Sc-doped NASICON, our results are different in terms of ionic conductivity. A much higher ionic conductivity can be achieved herein with different stoichiometry.^[20,21] Accordingly, it can be concluded that the number and distribution of Na ions, as well as phase structure are very important parameters to optimize for further increased ionic conductivity of NASICONs.

3. Conclusion

In this work, the influence of Sc^{3+} substitution on the local structures as well as the ionic motion of sodium ions has been revealed by XANES and SS-NMR study on a series of sodium-rich Sc-doped NASICON SSEs. XRD and XANES analysis show that Sc has been successfully doped in to NASICON to substitute Zr atoms, leading to a slight structural change. The NMR signals corresponding to Na2, Na1, and Na3, and impurities are resolved by fitting the spin-lattice relaxation time (T_1). It is determined that the distribution of sodium ions at different sites is directly responsible for the changes in ionic motion. In samples with $x \leq 0.3$, the reason for the acceleration of sodium ion movement is attributed to the increase of sodium ions at the Na2 sites and accompanying decrease at the Na1 and Na3 sites. For $x > 0.3$, the motion becomes sluggish because of the dramatic change in the distribution of sodium ions, which is caused by a phase change from monoclinic phase to rhombohedral phase. Insight into the mechanism and ion migration in the NASICON electrolyte can be of significance to inspire future study on sodium ion based SSEs and solid-state batteries.

4. Experimental Section

Materials Synthesis: Nominal compositions of $\text{Na}_{3+x}\text{Sc}_x\text{Zr}_{2-x}\text{Si}_2\text{PO}_{12}$ ($x = 0, 0.1, 0.2, 0.3, 0.4, 0.5, \text{ and } 0.6$), henceforth denoted as NSZSP x ($x = 0, 0.1, 0.2, 0.3, 0.4, 0.5, \text{ and } 0.6$), were synthesized by a sol-gel method using NaNO_3 ($\geq 99.0\%$, Sigma-Aldrich), Sc_2O_3 ($\geq 99.9\%$, Sigma-Aldrich), $\text{NH}_4\text{H}_2\text{PO}_4$ ($\geq 98\%$, Sigma-Aldrich), $\text{Si}(\text{OC}_2\text{H}_5)_4$ (tetraethyl orthosilicate, $\geq 98\%$, Sigma-Aldrich), $\text{C}_{12}\text{H}_{28}\text{O}_4\text{ZR}$ (zirconium(IV) propoxide solution, 70 wt% in 1-propanol, Sigma-Aldrich) as the starting materials, and citric acid as a chelating agent. First a mixture of tetraethyl orthosilicate, zirconium (IV) propoxide solution, citric acid, ethanol, and H_2O was stirred under 60°C over night. Then Sc_2O_3 was subjected to ultrasound in deionized water, 10% excessive of NaNO_3 and 10% excessive of $\text{NH}_4\text{H}_2\text{PO}_4$ and were dissolved into deionized water and then added to the previous solution. Afterwards, the collosol was heated at 70°C and always keeping stirring until a dried gel was achieved for several hours. Then, the dry xerogel thus obtained was first calcined in air at 500°C for 2 h and then at 1050°C for 10 h. The calcined powder was grounded and pressed into pellets (diameter 13 mm, thickness 3.5 mm) and sintered at 1250°C for 12 h. White ceramic pellets with a diameter between 11.2–11.5 mm and a thickness of around 3.2 mm can be obtained after sintering, demonstrating a considerable amount of shrinkage post-sintering.

Materials Characterization: The crystal structure and phase composition of NSZSP x ($x = 0, 0.1, 0.2, 0.3, 0.4, \text{ and } 0.5$) were investigated via the X-ray diffraction (XRD) using D8 Advance by Bruker with $\text{Cu K}\alpha$ X-ray source in the range of $10\text{--}70^\circ$ with a step of 0.01° per seconds. The scanning electron microscopy (SEM) pictures and energy dispersive spectrometer (EDS) mapping were taken using Hitachi 4800 SEM equipped with EDS detector. The working voltage employed for EDS mapping was 20 kV.

XAS Measurements: XAS measurements with fluorescence yield (FYI) modes of P K-edge, Si K-edge and Sc L-edge were performed on the soft X-ray micro characterization beamline (SXRMB) end station at Canadian Light Source (CLS) with powder samples. SXRMB was equipped with a double-crystal monochromator with two sets of interchangeable crystals InSb (111) and Si (111) under an operating energy range from 1.7 to 10 keV. All the XAS spectra were normalized to the incident photon flux and calibrated with the standard compound.

Electrochemical Measurement: The ionic conductivities of NSZSP x ($x = 0, 0.1, 0.2, 0.3, 0.4, 0.5, \text{ and } 0.6$) were measured by electrochemical impedance spectroscopy (EIS). Au electrodes were coated on the NSZSP x pellets by sputtering before conductivity measurement. Nyquist plots were recorded by a Gamry Electrochemical system in the frequency range of 100 mHz and 100 kHz with an AC voltage of 5 mV.

NMR Experiments: ^{23}Na MAS NMR spectra were acquired on an ultra-wide bore 900 MHz NMR spectrometer at the National High Magnetic Field Lab (NHMFL) using a home-made transmission line 3.2 mm MAS probe with a spinning rate of 10 kHz. ^{23}Na spin-lattice relaxation time (T_1) measurements, ^{29}Si , and ^{31}P MAS NMR spectra acquired on an AVANCE-400 Bruker spectrometer (9.4T) working at 105.9, 79.5, and 162.0 MHz respectively. A 4 mm Bruker MAS probe was employed for magic-angle spinning (MAS) experiments with spin rates of 12 kHz. The ^{23}Na T_1 time was determined using inversion recovery experiment. The chemical shift of ^{23}Na was referenced to aqueous 1 M NaCl solution (0 ppm). ^{29}Si and ^{31}P signals were recorded using direct polarization with a pulse length of 3 and 2.25 μs pulse. The chemical shifts of ^{29}Si and ^{31}P were referenced to Trimethylsilyl propanoic acid (0 ppm) and Ammonium dihydrogen phosphate (1 ppm). Recycle delays of $5 \times T_1$ were used for all experiments.

Supporting Information

Supporting Information is available from the Wiley Online Library or from the author.

Acknowledgements

F.S. and Y.X. contributed equally to this work. The work was supported by the National Science and Technology Major Project from Minister of Science and Technology of China (Grant no. 2018AAA0103104), National Natural Science Foundation of China (NSFC) (Grant nos. U1932124 and 21935009), the National Key R&D Program of China (Grant 2017YFA0205002), and the Priority Academic Program Development (PAPD) of Jiangsu Higher Education Institutions. This is also a project supported by the 111 Project, Joint International Research Laboratory for Carbon-Based Functional Materials and Devices and Collaborative Innovation Center of Suzhou Nano Science & Technology. This work is also supported by the Natural Science and Engineering Research Council of Canada (NSERC), the Canada Research Chair Program (CRC), the Canada Foundation for Innovation (CFI), and the University of Western Ontario (UWO). R.F. thanks to the support from the National High Magnetic Field Laboratory, which is supported by NSF Cooperative Agreement NSF/DMR-1644779 and the State of Florida.

Conflict of Interest

The authors declare no conflict of interest.

Data Availability Statement

Research data are not shared.

Keywords

diffusion mechanisms, high ionic conductivity, NASICON, NMR, Sc doping, solid-state electrolytes, XAS

Received: March 2, 2021

Revised: April 16, 2021

Published online:

- [1] D. Kundu, E. Talaie, V. Duffort, L. F. Nazar, *Angew. Chem. Int. Ed. Engl.* **2015**, *54*, 3431.
- [2] K. B. Hueso, M. Armand, T. Rojo, *Energy Environ. Sci.* **2013**, *6*, 734.
- [3] S. W. Kim, D. H. Seo, X. Ma, G. Ceder, K. Kang, *Adv. Energy Mater.* **2012**, *2*, 710.
- [4] V. Palomares, P. Serras, I. Villaluenga, K. B. Hueso, J. C. González, T. Rojo, *Energy Environ. Sci.* **2012**, *5*, 5884.
- [5] Y. Fang, L. Xiao, Z. Chen, X. Ai, Y. Cao, H. Yang, *Electrochem. Energy Rev.* **2019**, *1*, 294.
- [6] T. Wang, D. Su, D. Shanmukaraj, T. Rojo, M. Armand, G. Wang, *Electrochem. Energy Rev.* **2019**, *1*, 200.
- [7] J. B. Goodenough, *J. Solid State Electrochem.* **2012**, *16*, 2019.
- [8] Z. Zhang, Q. Zhang, J. Shi, Y. S. Chu, X. i. Yu, K. Xu, M. Ge, H. Yan, W. Li, L. Gu, Y. S. Hu, H. Li, X. Q. Yang, L. Chen, X. Huang, *Adv. Energy Mater.* **2016**, *7*, 1601196.
- [9] W. Zhao, J. Yi, P. He, H. Zhou, *Electrochem. Energy Rev.* **2019**, *2*, 574.
- [10] M. Weiss, F. J. Simon, M. R. Busche, T. Nakamura, D. Schroder, F. H. Richter, J. Janek, *Electrochem. Energy Rev.* **2020**, *3*, 221.
- [11] Z. Khakpour, *Electrochim. Acta* **2016**, *196*, 337.
- [12] Q. Ma, M. Guin, S. Naqash, C. L. Tsai, F. Tietz, O. Guillon, *Chem. Mater.* **2016**, *28*, 4821.
- [13] B. Xie, D. Jiang, J. Wu, T. Feng, J. Xia, H. Nian, *J. Phys. Chem. Solids* **2016**, *88*, 104.
- [14] A. G. Jolley, G. Cohn, G. T. Hitz, E. D. Wachsman, *Ionics* **2015**, *21*, 3031.
- [15] A. G. Jolley, D. D. Taylor, N. J. Schreiber, E. D. Wachsman, *J. Am. Ceram. Soc.* **2015**, *98*, 2902.
- [16] N. S. Bell, C. Edney, J. S. Wheeler, D. Ingersoll, E. D. Spoeke, *J. Am. Ceram. Soc.* **2014**, *97*, 3744.
- [17] R. O. Fuentes, F. M. Figueiredo, M. R. Soares, M. R. Soares, F. M. B. Marques, *J. Am. Chem. Soc.* **2005**, *25*, 455.
- [18] R. O. Fuentes, F. M. Figueiredo, F. M. B. Marques, J. I. Franco, *Solid State Ionics* **2001**, *140*, 173.
- [19] J. B. Goodenough, H. Y. P. Hong, J. A. Kafalas, *Mater. Res. Bull.* **1976**, *2*, 203.
- [20] Y. Deng, C. Eames, L. H. B. Nguyen, O. Pecher, K. J. Griffith, M. Courty, B. Fleutot, J. N. Chotard, C. P. Grey, M. S. Islam, C. Masquelier, *Chem. Mater.* **2018**, *30*, 2618.
- [21] S. Lunghammer, D. Prutsch, S. Breuer, D. Rettenwander, I. Hanzu, Q. Ma, F. Tietz, H. M. R. Wilkening, *Sci. Rep.* **2018**, *8*, 11970.
- [22] J. Yang, G. Liu, M. Avdeev, H. Wan, F. Han, L. Shen, Z. Zou, S. Shi, Y. S. Hu, C. Wang, X. Yao, *ACS Energy Lett.* **2020**, *5*, 2835.
- [23] Y. Shao, G. Zhong, Y. Lu, L. Liu, C. Zhao, Q. Zhang, Y. S. Hu, Y. Yang, L. Chen, *Energy Storage Mater.* **2019**, *23*, 514.
- [24] Z. Zhang, Z. Zou, K. Kaup, R. Xiao, S. Shi, M. Avdeev, Y. S. Hu, D. Wang, B. He, H. Li, X. Huang, L. F. Nazar, L. Chen, *Adv. Energy Mater.* **2019**, *9*, 1902373.
- [25] J. A. S. Oh, L. He, A. Plewa, M. Morita, Y. Zhao, T. Sakamoto, X. Song, W. Zhai, K. Zeng, L. Lu, *ACS Appl. Mater. Interfaces* **2019**, *11*, 40125.
- [26] Y. Ruan, S. Song, J. Liu, P. Liu, B. Cheng, X. Song, V. Battaglia, *Ceram. Int.* **2017**, *43*, 7810.
- [27] H. Park, K. Jung, M. Nezafati, C. S. Kim, B. Kang, *ACS Appl. Mater. Interfaces* **2016**, *8*, 27814.
- [28] J. S. Lee, C. M. Chang, Y. I. L. Lee, J. H. Lee, S. H. Hong, *J. Am. Ceram. Soc.* **2004**, *87*, 305.
- [29] K. Noi, K. Suzuki, N. Tanibata, A. Hayashi, M. Tatsumisago, *J. Am. Ceram. Soc.* **2017**, *101*, 1255.
- [30] Y. Shimizu, T. Ushijima, *Solid State Ionics* **2000**, *132*, 143.
- [31] M. Guin, F. Tietz, O. Guillon, *Solid State Ionics* **2016**, *293*, 18.
- [32] G. Kar, J. J. Schoenau, D. Hilger, D. Peak, *Can. J. Soil Sci.* **2017**, *97*, 626.
- [33] W. S. Yoon, K. Y. Chung, J. McBreen, K. Zaghbi, X. Q. Yang, *Electrochem. Solid-State Lett.* **2006**, *9*, A415.
- [34] R. Franke, J. Hormes, *Phys. B* **1995**, *216*, 85.
- [35] N. Okude, M. Nagoshi, H. Noro, Y. Baba, H. Yamamoto, T. A. Sasaki, *J. Electron Spectrosc. Relat. Phenom.* **1999**, *101*, 607.
- [36] J. Kruse, P. Leinweber, *J. Plant Nutr. Soil Sci.* **2008**, *171*, 613.